Article

Chloride Ion-Induced Spatial Separation and Long Recombination Time of Photogenerated Electrons and Holes in Crystalline Carbon Nitride

Xu Cai and Wei Lin*

Read Online

ACCESS | Metrics & More | Article Recommendations | SI Supporting Information

ABSTRACT: Poly(triazine imide)·Li$^+$Cl$^-$ (PTI/Li$^+$Cl$^-$) as one of the most reported crystalline carbon nitrides has shown exciting potential for photocatalysis. However, understanding the role of Li$^+$/Cl$^-$ in the photoexcited charge transfer in the time and space of PTI is a challenging problem. Here, we have investigated the nonradiative charge recombination of series ion intercalated PTI systems (PTI/Li$^+$X$^-$, where X = F, Cl, Br, and I) by performing the *ab initio* nonadiabatic molecular dynamics simulations. The results indicate that the intercalated anions in PTI/Li$^+$Cl$^-$ and PTI/Li$^+$Br$^-$ have the potential to trap holes, separate the electrons and holes, and prolong the nonradiative electron−hole recombination. In particular, ∼70% of holes in PTI/Li$^+$Cl$^-$ can transport among interlayers toward the {0001} planes, while most of the electrons are transferred to the {10$\bar{1}$0} planes, exhibiting different transport pathways and directions. Furthermore, PTI/Li$^+$Cl$^-$ has an electron−hole recombination time as long as 136 ns, which explains its excellent optoelectronic properties. This work provides a theoretical baseline for the reported facet engineering improvement of crystalline carbon nitride for overall water splitting.

KEYWORDS: crystalline carbon nitride, lithium halide, spatial separation of electron and hole, charge carrier lifetime, recombination time
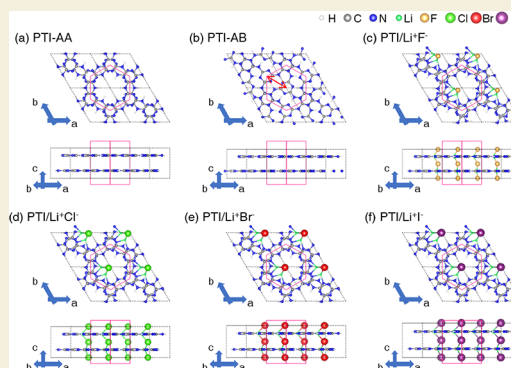
INTRODUCTION

Over the past few decades, concerns about environmental pollution and energy shortages caused by the extensive use of oil have led people to search for cleaner and more sustainable energy sources. In 2009, Wang et al. proposed the application of carbon nitride (CN) in photocatalysis.[1] Due to its affordable, easy-to-synthesize, and metal-free nature, CN has been extensively explored. Various types of CNs have been synthesized and applied in photocatalysis and many fields, such as triazine-based g-C$_3$N$_4$, melon, polyheptazine imide (PHI), and polytriazine imide (PTI). The synthesis of a structurally well-characterized CN is difficult, which hinders in-depth research into CN. Among the various types of CNs, the ion intercalated PTI, e.g., PTI/HCl, PTI/Li$^+$Cl$^-$, and PTI/Li$^+$Br$^-$, synthesized by an ionothermal and molten salt method has a highly crystalline and hold immense promise within the field of photochemistry, particularly in endeavors such as overall water splitting, as well as possessing commendable optoelectronic properties.[2−5] The triazine-based CN layers, characterized by triangular pores, are arranged in an alternating fashion within the ion intercalated PTI. The ions infiltrate these pores, acting as a skeletal framework that holds the CN layers together, ultimately forming a hexagonal prism structure. In the PTI structure, the cations reside at the corners of the triangular pores and are coplanar with the CN layers. Conversely, the anions occupy the central position within the pores and are situated in the middle of the interlaminar spaces. The lithium and chlorine intercalated PTI (PTI/Li$^+$Cl$^-$) have been widely studied due to its high photocatalysis activity.[6−8] Elemental analysis and quantitative NMR spectroscopy demonstrated the disorder H/Li structure in PTI/Li$^+$Cl$^-$.[9] Research on the H/Li substructure has shown that the optical properties of PTI/Li$^+$Cl$^-$ are susceptible to the H/Li substructure. The characterization of light elements has presented a formidable challenge for the further understanding of the substructure of PTI; recent advances have made it possible to explore it in greater depth.[10−13] Excitingly, Genoux and colleagues recently achieved substantial photocatalytic performance and photoconductivity in PTI/FeCl$_2$ by replacing Li with Fe.[14] In contrast to cations, anions have definite structural information. Recent studies have shown that the different types of anions in PTI have a significant impact on its optical properties, such as
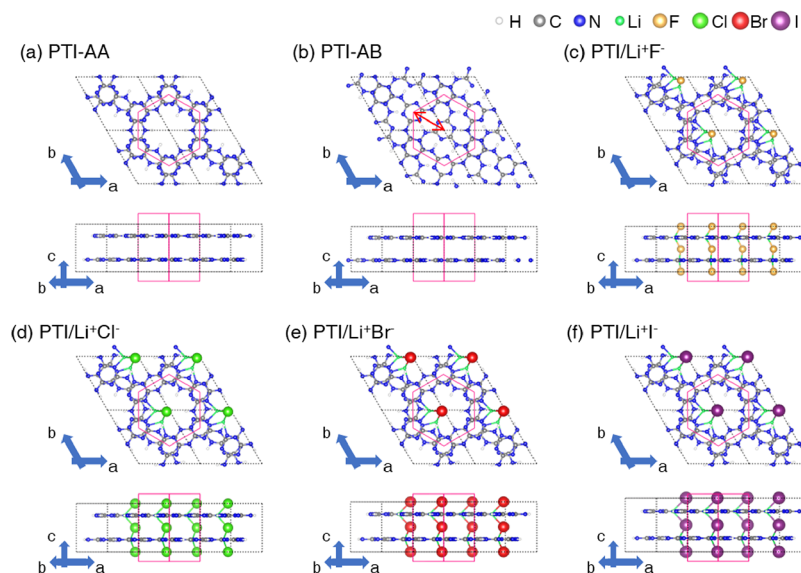
Figure 1. Crystal structural models of (a) PTI-AA, (b) PTI-AB, (c) PTI/Li$^+$F$^-$, (d) PTI/Li$^+$Cl$^-$, (e) PTI/Li$^+$Br$^-$, and (f) PTI/Li$^+$Cl$^-$. The pink frame depicts the hexagonal tunnel of PTI. The red arrow in panel b indicates the displacements of the second CN layer relative to the first layer in PTI-AB.

its absorption spectrum and luminescence.[15−17] Studying the specific effects of different ions in PTI is helpful to improve performance of PTI. Note that only crystalline structures of PTI/Li$^+$Cl$^-$ and PTI/Li$^+$Br$^-$ have been synthesized via the molten salt method, while large I$^-$ leads to the formation of the heptazine-based hydrogen-bonded melem hydrate as the main crystalline phase.[15,16] Furthermore, it is reported that treatment of PTI/Li$^+$Br$^-$ with concentrated ammonium fluoride yields PTI with intercalated fluoride ions (PTI/Li$^+$F$^-$) as a statistical phase mix with PTI/Li$^+$Br$^-$.[15]

Ion exchange could change the species of the ions in PTI and maintains the prism structure,[13] which allows us to obtain more PTI intercalated with different types of ions. The ion intercalated PTI has a structure that contains both CN layers and an ion skeleton. It shares similarities with recently popular metal−organic framework (MOF) materials and hybrid organic−inorganic perovskites, which are believed to have the potential to separate photogenerated *e-h* pairs and extend the charge carrier's lifetime.[18,19] For example, electrons and holes can be separated through capture by different parts of the material or by induction from the disordered cation orientation. The two independent components of PTI, i.e., the CN layers and ion skeleton, may have the same potential for charge separation. Hence, the study of the ion substructure of PTI is crucial for its future development.

In this work, we have investigated the effect of anions on photogenerated carriers by comparing a series PTI/Li$^+$X$^-$ (X = F, Cl, Br, and I) and pristine PTI without ion intercalation. By using the state-of-the-art nonadiabatic molecular dynamics (NAMD) program, Hefei-NAMD,[20] the charge separation and recombination of various PTI are compared. The results indicate that PTI/Li$^+$Cl$^-$ has the longest charge carrier's lifetime, which can be attributed to the suitable anion radius and energy levels of Cl$^-$. The charge separation delays the *e-h* recombination and extends the charge carrier's lifetime in both PTI/Li$^+$Cl$^-$ and PTI/Li$^+$Br$^-$. Since the induced energy levels are below the VBM of the CN layers, F$^-$ is unable to capture the hole in PTI/Li$^+$F$^-$. Furthermore, PTI/Li$^+$I$^-$ exhibits the shortest recombination process due to the large anion radius of

I$^-$ and the small band gap value caused by the high energy levels of I$^-$. In addition, it is interesting to see that the holes trapped by anions exhibit transport properties different from those of excited electrons. The trapped holes exhibit significant anisotropy by transporting in both perpendicular and vertical directions. This property gives ion intercalated PTIs a great potential for facet engineering modification.

COMPUTATIONAL METHODS

DFT Calculations

All density functional theory (DFT) calculations were done through the Vienna *ab initio* simulation package (VASP) version 5.4.[21−23] Projector augmented wave (PAW) potentials[24] were used to describe the electron−ion interactions, and the generalized gradient approximation (GGA) of Perdew, Burke, and Ernzerhof (PBE) functional was used to describe the exchange and correlation interactions.[25] Heyd-Scuseria-Ernzerhof (HSE06) functional was also used in the density of states (DOS) calculations for comparison.[26] The van der Waals corrections were considered via Grimme's D3 method. The wave function was expanded using plane waves with a cutoff energy of 520 eV. The Brillouin zone was sampled with a $3 \times 3 \times 4$ k-mesh for geometry optimization and $6 \times 6 \times 8$ for self-consistent calculations in the primitive cell, respectively. The systems were fully relaxed until the self-consistency energy difference was smaller than 10^{-6} eV, and the Hellmann−Feynman forces were smaller than 0.01 eV/Å in optimization.

Binding Energy

The stability is evaluated by modification of the binding energy (E_b). Since the differences between PTI systems come from the interlayer structure between CN layers and ion species and PTI/Li$^+$X$^-$ is mostly synthesized by lithium halide salts (Li-X), we consider the following reactions in one unit cell:

$$2LiX + 2[C_6N_9H_3] \rightarrow [C_6N_9H_3]_2 \cdot 2[Li^+X^-] \tag{1}$$
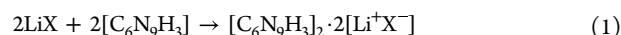
Therefore, the binding energy per unit cell E_b of PTI/Li$^+$X$^-$ is

$$E_b = E_{PTI/Li^+X^-} - 2E_{PTI\_monoalyer} - 2E_{LiX} \tag{2}$$

For PTI without ions:

$$2[C_6N_9H_3] \rightarrow [C_6N_9H_3]_2 \tag{3}$$

the binding energy per unit cell E_b of PTI without ions:

$$E_b = E_{PTI} - 2E_{PTI\_monolayer} \tag{4}$$

where the E_{PTI/Li^+X^-} and E_{PTI} are the potential energies of bulk PTI systems; $E_{PTI\_monolayer}$ is the potential energy of monolayer PTI. E_{LiX} is the potential energies of bulk of the corresponding lithium halide salts.

AIMD Simulation

A $\sqrt{3} \times \sqrt{3} \times 2$ supercell and Γ point are used in the AIMD simulations. Considering the Li^+ cation occupies the vacancy of the pore of CN layer with 1/3 probabilities, the supercell is constructed, as shown in Figure S1. The AIMD simulations were carried out in the microcanonical ensemble (NVE) under 300 K with a 1 fs/step time step for at least 10 ps. After the system stabilized, the last 6 ps of the trajectory were collected for the NAMD calculations.

NAMD Simulation

The NAMD simulations were performed with the decoherence-induced surface hopping (DISH) method implemented within the time-dependent Kohn–Sham density functional theory.[27] To reduce the computational cost of a long time NAMD simulation, the kinetic method from the previous report was adopted.[28] The short-time NAMD simulations in the hole trapping and e-h recombination dynamics were carried out to obtain the transition rates for every pair of key states. The long time hole trapping and e-h recombination dynamics simulation were performed by solving the coupled kinetic equations, as shown in the eqs S5–S20 in the Supporting Information.

Effective Mass

The effective masses are calculated from the band structures of primitive cells of each system through the finite difference method.

■ RESULTS AND DISCUSSION

Geometric Structure

Note that PTI/Li$^+$F$^-$ and PTI/Li$^+$I$^-$ were not synthesized in experiments. However, to explore the effect of halogen anions on the functionality and charge carrier lifetime of PTI, we have examined four PTI/Li$^+$X$^-$ systems, where X represents F, Cl, Br, and I. Additionally, we considered two pristine PTI systems without ion intercalation. One preserved the hexagonal tunnel structure, labeled PTI-AA, while the other exhibited interlayer displacement and was labeled PTI-AB. The optimized geometries are shown in Figure 1. The CN layers are held by van der Waals interactions and $\pi-\pi$ stackings, which are further stabilized by the Li$^+$X$^-$ skeleton, leading to the formation of a hexagonal lattice. Table 1 summarizes the average interlayer distance ($<D>$) of CN layers, the binding energy (E_b) of PTI-AB, PTI-AA, and PTI/Li$^+$X$^-$ systems. Due

to the strong electrostatic repulsion between the triazine unit, PTI-AA exhibits a slightly higher E_b (−0.605 eV/unit) compared to PTI-AB (−0.618 eV/unit). The interlayer displacement in PTI-AB reduces the electrostatic repulsion and thereby the interlayer spacing, which is consistent with previous report of Chi et al.[29] The ions within the PTI play a significant role in stabilizing the structure of the CN layer. Upon losing these ions, the CN layer within the PTI tends to undergo translational movement to mitigate electrostatic repulsion.[29] The interlayer distances of PTI-AB, PTI/Li$^+$Cl$^-$, and PTI/Li$^+$Br$^-$ obtained in this work are consistent with the experiments.[4,15,30] Generally, the interlayer distance is heavily influenced by the radius of the anion. PTI/Li$^+$F$^-$ exhibits a smaller interlayer distance compared to PTI-AA and is close to PTI-AB due to the strong Li–F bond bringing the CN layers closer together. The small interlayer distance increases electrostatic repulsion among the CN layers, resulting in the highest E_b value of −0.605 eV/unit and an unstable structure. Chong et al. reported challenges in directly synthesizing PTI/Li$^+$F$^-$ with a crystalline structure similar to that of PTI/Li$^+$Cl$^-$.[15] PTI/Li$^+$Cl$^-$ and PTI/Li$^+$Br$^-$ have little change on the interlayer distance due to their comparable anion diameters (Cl$^-$ is 3.34 Å and Br$^-$ is 3.64 Å) to the interlayer distances in the pristine PTI (3.32 Å). The interlayer distance increases by only 0.06 and 0.16 Å, respectively. Conversely, PTI/Li$^+$I$^-$ experiences a larger increase in the interlayer distance by 0.45 Å, attributed to the larger anion diameter of the I$^-$ anion (4.12 Å). This increase of interlayer distance reduces the interlayer interaction between CN layers, rendering the system unstable. Burmeister et al. reported the effect of different sizes of anions (Cl, Br, I) on the structure of PTI, which demonstrated that PTI/Li$^+$I$^-$ is thermodynamically unstable and the heptazine (C$_6$N$_7$)-based hydrogen-bonded melem hydrate is formed as the main crystalline phase.[16]

The root-mean-squared fluctuation (RMSF) during the 6 ps *ab initio* molecular dynamics (AIMD) simulation of CN layers, lithium and anion of the systems at 300 K, is summarized in Table 1. Additionally, Figure 2 illustrates the atom distribution of the PTI/Li$^+$X$^-$ systems throughout the MD simulation. Both quantify the extent of thermal motions. The absence of ions causes the CN layers to experience increased sliding, resulting in greater RMSF values for the CN layer positions in PTI-AA and PTI-AB compared to those in PTI/Li$^+$X$^-$. The potential energy surface (PES) associated with the interlayer displacement of PTI, as illustrated in Figure S2a, reveals small energy barriers between PTI-AA and PTI-AB, indicating that the CN layers in PTI exhibit a propensity for facile sliding. The trajectories of interlayer displacements for PTI-AA and PTI-AB, depicted in Figure S2b–e, reveal that, in PTI-AA, the interlayer structures of CN layers quickly become disordered due to thermal motion, resembling a misaligned layer structure similar to that of PTI-AB. It can be seen that the intercalation of ions plays a crucial role in stabilizing the hexagonal shape of PTI. The RMSF of CN layers in PTI/Li$^+$F$^-$ is the smallest due to the limited out-of-plane fluctuations caused by the small interlayer spacing. Both F$^-$ and I$^-$ exhibit smaller RMSF values compared to Cl$^-$ and Br$^-$, demonstrating limited variations. The strong Li–F bond caused F$^-$ to be located close to Li$^+$ and away from the center of the pore of the CN layer (Figure 2a), while the large anion radius of I$^-$ restricted its position within the center (Figure 2d). On the other hand, Cl$^-$ and Br$^-$, with intermediate-sized anions and greater freedom of motion (Figure 2b,c), result in the larger RMSF values than those of

Table 1. Average Interlayer Distance ($<D>$), Binding Energy (E_b), and Root-Mean-Square Fluctuation (RMSF) of PTI-AA, PTI-AB, and PTI/Li$^+$X$^-$ (X = F, Cl, Br, and I)

model	$<D>$ (Å)	E_b (eV/unit)	RMSF (Å)		
			CN layer (C, N, and H)	anion	Li
PTI-AA	3.16	−0.605	1.422		
PTI-AB	3.32	−0.618	1.025		
PTI/Li$^+$F$^-$	3.16	−0.208	0.292	0.453	0.434
PTI/Li$^+$Cl$^-$	3.38	−0.807	0.317	0.535	0.556
PTI/Li$^+$Br$^-$	3.48	−0.906	0.325	0.477	0.482
PTI/Li$^+$I$^-$	3.77	−0.956	0.321	0.387	0.377
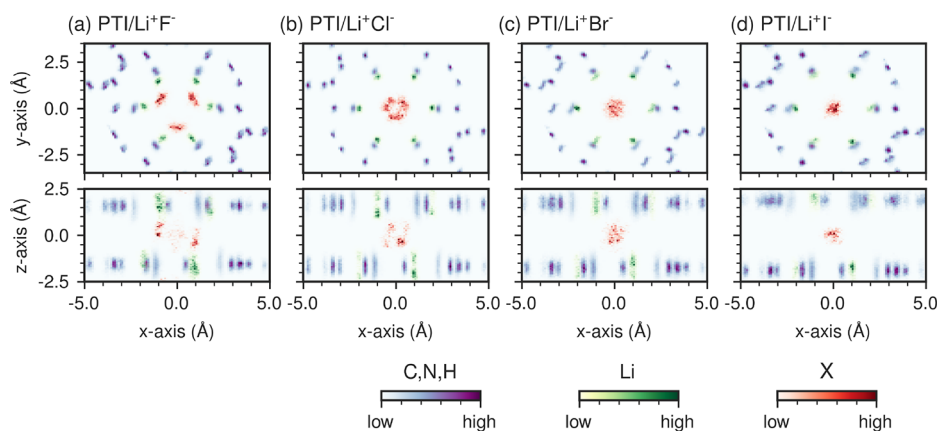
Figure 2. Atomic distribution during the AIMD simulations of (a) PTI/Li$^+$F$^-$, (a) PTI/Li$^+$Cl$^-$, (c) PTI/Li$^+$Br$^-$, and (d) PTI/Li$^+$I$^-$. The blue, green, and red colors denote the special distribution of CN layers (C, N, H), Li$^+$, and anion, respectively.
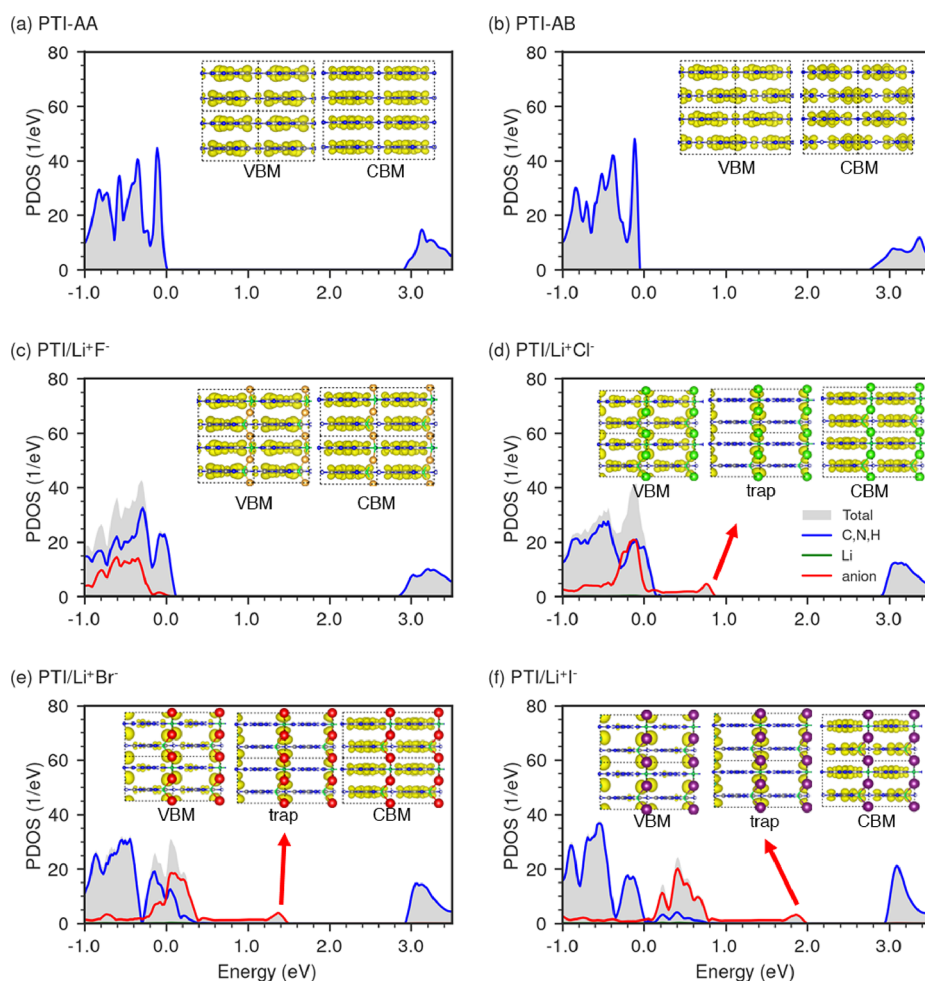

Figure 3. Projected density of states using PBE functional of (a) PTI-AA, (b) PTI-AB, (c) PTI/Li$^+$F$^-$, (d) PTI/Li$^+$Cl$^-$, (e) PTI/Li$^+$Br$^-$, and (f) PTI/Li$^+$I$^-$. The insets show the charge densities of the VBM, CBM, and trap states. The isovalue is set to 0.003 Bohr/Å^{-3}. For comparison, the energy levels of different systems have been aligned with the VBM level of PTI-AA set at 0 eV.

F$^-$ and I$^-$. In addition, the variations of Li$^+$ and anions show similar trends distinct from those observed in the CN layers. This suggests that the Li-X and CN layers are structurally independent of each other, each possessing its own motion characteristics. The distinct motion characteristics of Li-X and CN layers can lead to rapid dephasing between their associated

states, thereby inhibiting *e-h* recombination when the electron and hole are localized separately on the CN layer and Li-X.

Electronic Structure

Figure 3 shows projected densities of states (PDOS) for the PTI-AA, PTI-AB, and PTI/Li$^+$X$^-$ systems. To facilitate the description and contrast of the role of ions in PTI, we refer to the top of the valence band of the continuums in which the
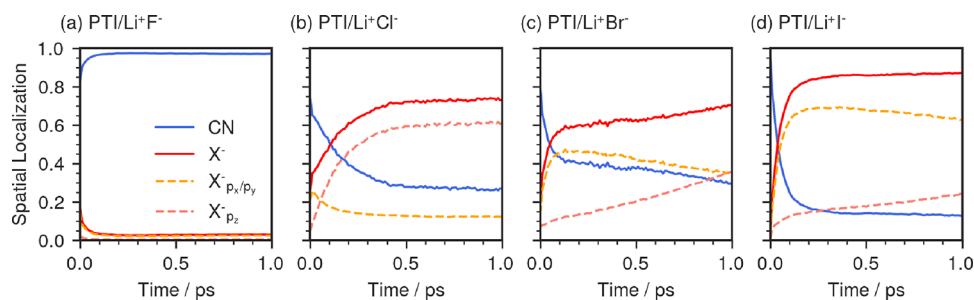
Figure 4. Time-dependent spatial hole localization of (a) PTI/Li$^+$F$^-$, (b) PTI/Li$^+$Cl$^-$, (c) PTI/Li$^+$Br$^-$, and (d) PTI/Li$^+$I$^-$.
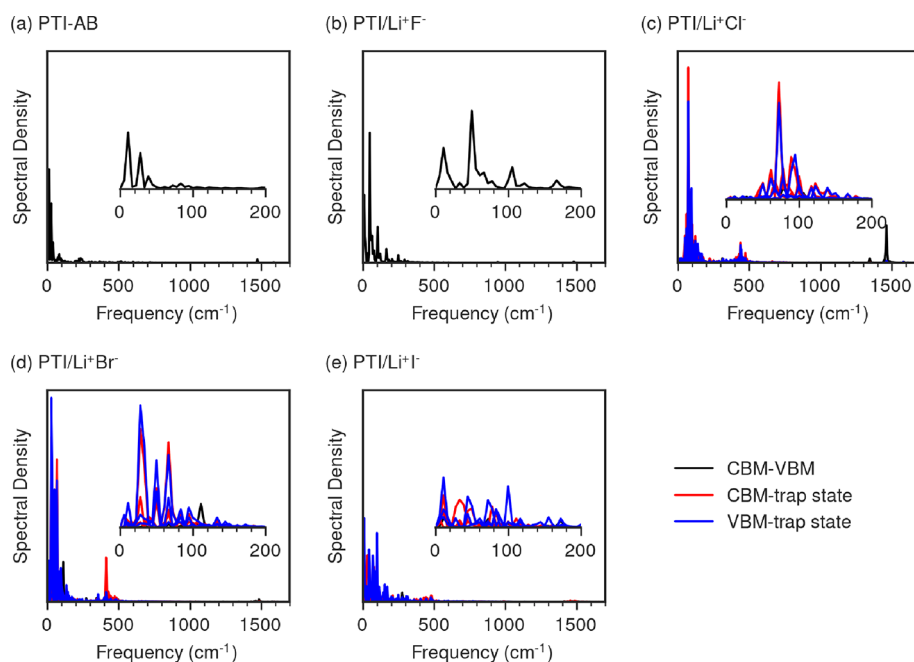

Figure 5. Pure-dephasing functions for the key pairs of states for recombination and hole trapping in (a) PTI-AB, (b) PTI/Li$^+$F$^-$, (c) PTI/Li$^+$Cl$^-$, (d) PTI/Li$^+$Br$^-$, and (e) PTI/Li$^+$I$^-$.

CN layers participate as the valence band minimum (VBM) of the PTI/Li/X$^-$ system. In the middle of the band gap, an occupied state formed by the p$_z$ orbital of anions serves as a hole trap state. The insets in Figure 3 show the spatial charge densities of the VBM, conduct band minimum (CBM), and the trap state induced by Li-X. The PDOS and charge densities calculations are also performed using the HSE06 functional, which is commonly used to describe the electronic properties of semiconductors. The HSE06 results are presented in Figure S3 and both HSE06 and PBE results present similar trends in the energy gaps and charge densities. The light absorption of PTI/Li$^+$Cl$^-$ mainly comes from the contribution of CN. Compared with the observed optical gap in the experiment of PTI/Li$^+$Cl$^-$, which is around 3.1 eV,[6,31] the PBE functional provides more accurate optical bandgap results, while the HSE functional is overestimated by about 1.0 eV. This result is consistent with the previous theoretical reports that pointed out the challenges of correctly estimating the optical gaps of carbon nitride materials.[31,32]

PTI-AB exhibits a modestly increased band gap compared to PTI-AA due to the electrostatic repulsion between the layers. Around the Fermi level, the impact of intercalation of Li-X primarily manifests in the VB. The intercalation of ions has little effect on the characteristics of CB. The energy levels of states associated with anions shift upward overall, as the attraction between anions and outer electrons weakens with an increasing anion radius. The states associated with F$^-$ are located below the VBM of CN layers (Figure 3c). In PTI/Li$^+$Cl$^-$, PTI/Li$^+$Br$^-$, and PTI/Li$^+$I$^-$, the increase in the energy level of the anion state introduces an occupied state in the middle of the band gap (Figure 3d−f), which has the potential to trap holes, consequently influencing the e-h recombination process. In addition to the introduction of the hole trapping state, in PTI/Li$^+$Br$^-$ and PTI/Li$^+$I$^-$, the major component of the VBM in the continuum changes from the N atoms of the CN layer to the anions. Due to the higher energy states occupying the VBM, the VBM-CBM gap in PTI/Li$^+$Br$^-$ and PTI/Li$^+$I$^-$ is much smaller than that in PTI-AA, whereas the VBM-CBM gap in PTI/Li$^+$Cl$^-$ and PTI/Li$^+$F$^-$ exhibits a smaller decrease. Generally, the intercalation of ions introduces new states into the VB of PTI near the Fermi level, potentially influencing the behavior of holes within PTI. Specifically, in PTI/Li$^+$Cl$^-$, PTI/Li$^+$Br$^-$, and PTI/Li$^+$I$^-$, the induced hole trapping state is localized on the anions, while the CBM is localized on the CN layers, which facilitates the separation of electron and hole, extending the lifetime of charge carriers.
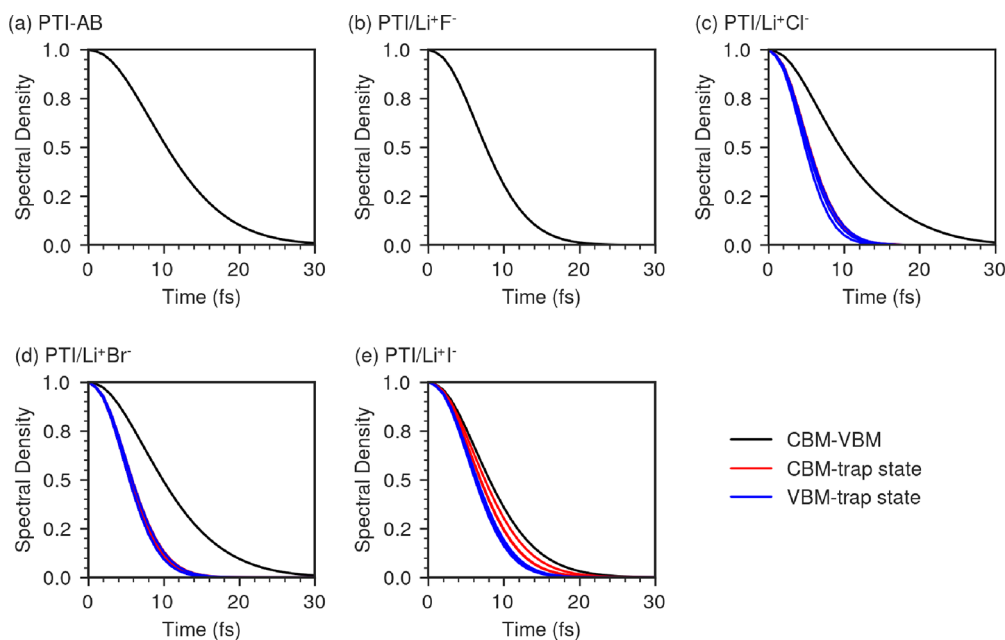
Figure 6. Pure-dephasing functions for the key pairs of states for hole trapping and recombination in (a) PTI-AB, (b) PTI/Li⁺F⁻ (c) PTI/Li⁺Cl⁻, (d) PTI/Li⁺Br⁻, and PTI/Li⁺I⁻.

Hole Trapping and Charge Separation

To verify whether the holes can be trapped by anions, we performed a nonadiabatic dynamic simulation of the holes in the anion-embedded PTI system, and the holes were initially set to the state of CN layers to investigate the dynamics of the holes from CN layers to anions. Both HSE06 and PBE functionals exhibit the same electronic characteristics of the key states related to the hole trapping and *e-h* recombination. Given the high computational cost of NAMD simulation, we use the PBE functional for subsequent calculations.

Figure 4 illustrates the hole transfer dynamics results in different systems. No hole transfer occurs in PTI/Li⁺F⁻ because the energy levels of states associated with F⁻ are lower than those of the states of CN layers (Figure 4a). The hole transfer in PTI/Li⁺Cl⁻ takes approximately 400 fs until the hole distribution on Cl⁻ and CN layers converges to 70 and 30%, respectively (Figure 4b). Since the energy levels of Cl⁻'s p_x/p_y orbitals are slightly lower than the states associated with CN layers, holes in PTI/Li⁺Cl⁻ are not initially transferred to the Cl⁻'s p_x/p_y orbitals but are directly transferred from CN layers to the Cl⁻'s p_z orbital. Therefore, there is only one stage of hole transfer in PTI/Li⁺Cl⁻. The hole transfer in PTI/Li⁺Br⁻ and PTI/Li⁺I⁻ takes two stages (Figure 4c,d). First, the hole rapidly transfers to the VBM within 100−150 fs, which is a hybridization of CN layers and anion's p_x/p_y orbitals. The distribution of holes on anions increases to 60 and 80% in PTI/Li⁺Br⁻ and PTI/Li⁺I⁻, respectively. Then, a slow process ensues where the holes from anions' p_x/p_y transfer to anions' p_z orbital, this process lasts on a time scale of tens of picoseconds.

Electron-Vibrational Interactions

Given the second stage of hole transfer in PTI/Li⁺Br⁻ and PTI/Li⁺I⁻ involves a lengthy transfer time, and that holes in PTI/Li⁺Cl⁻ still have a 30% distribution in CN layers after convergence, two pathways are taken into account in the recombination process: VBM-CBM recombination and trap-CBM recombination, both of which are considered in the

recombination simulations. To identify the phonon modes involved in the charge trapping and recombination, Figure 5 depicts the Fourier transform (FT) of the unnormalized autocorrelation function (ACF) for the energy difference of each pair of key states, which is also referred to as the spectral densities. In comparison to PTI-AA, PTI-AB exhibits a more stable structure, the experiment's reports also reported that PTI-AB is the most possible structure of PTI without ion intercalated.[29] Consequently, PTI-AB is employed as a structural reference for pristine PTI in the NAMD simulation to investigate the impact of ion intercalation in PTI. The spectral density of the energy difference reflects the phonon modes involved in the transition between states. The high density demonstrates rapid dephasing between the key states, which suppresses the transition between states. The spectral densities in all systems exhibit signals in the low frequency below 500 cm⁻¹. Phonon modes at these frequencies contribute strongly to electron-vibrational coupling in these systems. Two typical phonon modes are observed at around 10−100 cm⁻¹ range, which correspond to the CN layer out-of-plane fluctuations and anion vibrations, respectively. The frequencies of the anion vibration are negatively correlated with the anion mass. The high frequency vibration modes at 1500 cm⁻¹ are attributed to the C−N−C vibrations. The close interaction between CN and the Li−F skeleton affects the variation mode of CN and exhibits higher spectral densities and gap fluctuations. This causes a shift of the signal in PTI/Li⁺F⁻ toward higher frequencies and amplitudes. The peak at 400 cm⁻¹ is attributed to the collective vibration of Li cations and CN layers, which is restricted in PTI/Li⁺F⁻ and PTI/Li⁺I⁻ since the limited motion of Li-X in those systems, leading to a decrease in spectral density. That is consistent with the low RMSF values of Li as discussed in Table 1. In contrast, PTI/Li⁺Cl⁻ and PTI/Li⁺Br⁻ provide additional freedom for Cl⁻ and Br⁻ anion vibrations, intensifying the intensities in these systems. The high spectral density results in a large gap fluctuation and fast dephasing between the related states.

Table 2. Averaged Energy Gaps, NACs, Pure-Dephasing Times, Gap Fluctuations, and Transition Rates of Each State Pair between Key States of PTI-AB and PTI/Li$^+$X$^-$ (X = F, Cl, Br, and I)

model	state pair	energy gap @300 K (eV)	NAC (meV)	dephasing (fs)	gap fluctuation (eV^2)	transition rate (ns^{-1})
PTI-AB	VBM/CBM	2.79	0.45	9.0	0.0073	0.0211
PTI/Li$^+$F$^-$	VBM/CBM	2.48	0.46	6.5	0.013	0.0343
PTI/Li$^+$Cl$^-$	VBM/CBM	2.40	0.35	8.6	0.0099	0.0166
	trap/CBM	2.01	0.14	4.6	0.026	0.00352
	VBM/trap	0.40	5.48	4.4	0.027	1672, 688^a
PTI/Li$^+$Br$^-$	VBM/CBM	2.28	0.26	8.6	0.0088	0.00947
	trap/CBM	1.36	0.19	4.8	0.024	0.0165
	VBM/trap	0.92	1.47	4.8	0.023	37.8
PTI/Li$^+$I$^-$	VBM/CBM	1.91	0.25	7.0	0.012	0.0195
	trap/CBM	0.89	0.39	6.1	0.016	0.373
	VBM/trap	1.03	1.41	5.4	0.018	21.3

^{a}The transition rate of the VBM/trap of PTI/Li$^+$Cl$^-$ denotes $k_{\text{VBM}\rightarrow\text{trap}}$ and $k_{\text{trap}\rightarrow\text{VBM}}$, respectively, since the rate of $k_{\text{trap}\rightarrow\text{VBM}}$ cannot be neglected in PTI/Li$^+$Cl$^-$.
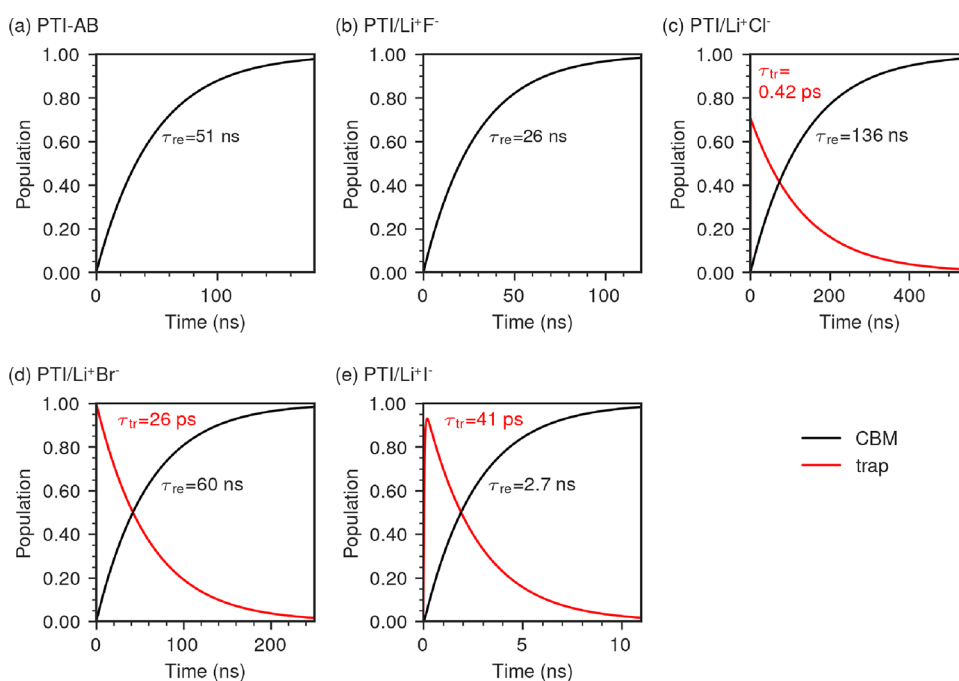

Figure 7. Evolution of populations of the key states in (a) PTI-AB, (b) PTI/Li$^+$F$^-$, (c) PTI/Li$^+$Cl$^-$, (d) PTI/Li$^+$Br$^-$, and (e) PTI/Li$^+$I$^-$. The annotated number represents the time that it takes for hole transfer (τ_{tr}) and e-h recombination (τ_{re}).

The pure-dephasing functions of key state pairs, computed from the optical response theory using second-order cumulant expansion, are presented in Figure 6. These functions provide insight into the decoherence between the key states within the systems. Fitting the dephasing function to a Gaussian function, $D(t) = \exp(-0.5(t/\tau)^2)$, yields the pure-dephasing time, which is presented in Table 2. In PTI-AB, the pure-dephasing time between the VBM and CBM is approximately 9 fs. While in PTI/Li$^+$F$^-$, involving Li−F interactions, the dephasing between VBM and CBM is much faster (6.5 fs). Both PTI-AB and PTI/Li$^+$F$^-$ have the same CN layer component in VBM and CBM. The dephasing time between the trap state and CBM ranges from 4 to 6 fs in PTI/Li$^+$Cl$^-$, PTI/Li$^+$Br$^-$, and PTI/Li$^+$I$^-$. This dephasing time is much faster compared to that between the VBM and CBM in all systems, which means that the introduction of trap states will accelerate the dephasing of electrons and hole. The fast dephasing causes an intriguing phenomenon known as the "quantum Zeno effect". This effect, in turn, significantly delays the state changes within

the system, ultimately resulting in a pronounced increase in the recombination time.

e-h Recombination

The separation of electrons and holes contributes to prolonging the lifetime of photoexcited carriers, which is advantageous for improving the performance of materials in applications such as photocatalysis or photochemistry. The nonradiative e-h recombination simulation of PTI systems with different ion intercalations was carried out by using the decoherence included surface hopping (DISH) method. To reduce computational costs, we adopted a kinetic method to describe the hole trapping and e-h recombination processes in PTI systems. The method has been successfully applied in previous reports.[28] The method gives the evolution of population on a long time scale by solving the corresponding kinetic equations (eqs S5−S20). The transition rates between key states in the kinetic equations are obtained by fitting the short-time scale NAMD simulation results (Figures S4−S7) to

the exponential function and are presented in Table 2. The evolution of the populations of the key states in the kinetic simulations is shown in Figure 7.

The average nonadiabatic coupling (NAC) and energy gap of key state pairs summarized in Table 2 can help us further explore how the induced hole trap states affect the electron−hole recombination process in PTI. For PTI-AB and PTI/Li⁺F⁻, the *e-h* recombination occurs in the CN layers, exhibiting almost the same nonadiabatic coupling (NAC) as shown in Table 2. Although the involvement of Li−F accelerates the dephasing of the system, the reduction of the band gap accelerates the *e-h* recombination in PTI/Li⁺F⁻. Hole trapping occurs rapidly in PTI/Li⁺Cl⁻ and PTI/Li⁺Br⁻ and in PTI/Li⁺I⁻. Therefore, the *e-h* recombination is majorly determined by the transition between the trap states and CBM in these systems. It shows that the intercalation of ions successfully separated the electrons and holes. The transition between the trap state and CBM has a smaller NAC and faster dephasing than the transition between VBM and CBM, which inhibits the *e-h* recombination process. However, in PTI/Li⁺I⁻, the improvement in NAC and dephasing time is limited. In contrast, the energy gap between trap and CBM in PTI/Li⁺I⁻ is very narrow (0.89 eV) and extremely speedup the transition rate, resulting in the shortest *e-h* recombination time (2.6 ns). In PTI/Li⁺Cl⁻ and PTI/Li⁺Br⁻, the loose structure results in a significant reduction in NAC and pure-dephasing time. Furthermore, the reduction in their energy gap is comparatively smaller when compared to that of PTI/Li⁺I⁻. As a result, the *e-h* recombination times in these systems are extended. Among the two, PTI/Li⁺Cl⁻ exhibits a smaller NAC, faster dephasing as well as a larger energy gap between the trap state and CBM, leading the longest *e-h* recombination time that is three times longer than that of PTI-AB.

Anisotropy of Carrier Transport

As previously stated, upon formation of electron−hole pairs, the holes are promptly captured by the anions, while the electrons remain within the CN layers. The free charge carriers, prior to recombination, drift and diffuse within the crystal and migrate to the surface, triggering oxidation or reduction reactions. The different distributions of excited holes and electrons lead to differences in the transport behaviors. Table 3 shows the components of the effective masses of holes

Table 3. Effective Masses of Hole and Electron at the VBM and CBM in Different Systems

model	CBM (m_0)			VBM (m_0)		
	m_x	m_y	m_z	m_x	m_y	m_z
PTI-AA	1.68	1.68	1.52	−2.09	−2.09	−15.12
PTI-AB	0.41	1.34	2.45	−3.99	−2.81	−71.21
PTI/Li⁺F⁻	1.56	1.26	1.46	−3.88	−2.89	−123.69
PTI/Li⁺Cl⁻	1.81	4.14	1.77	−41.65	−74.20	−0.47
PTI/Li⁺Br⁻	0.77	9.72	3.06	−35.52	−289.95	−0.31
PTI/Li⁺I⁻	0.76	1.62	37.28	−18.19	−29.78	−0.22

and electrons in the CBM and VBM in three directions. The effective masses were determined from the electronic band structures of the primitive cells of each system (Figure S8). The supercells constructed for NAMD simulation have different Li ion distributions compared to the primitive cells. Therefore, the effective band structures (EBS) of the supercells were also calculated for comparation and are depicted in

Figure S9. Upon comparing the band structures of the supercells with that of the primitive cells, the different Li distributions have a minimal impact. Notably, electrons and holes exhibit significant differences in various directions.

In PTI-AA, PTI-AB, and PTI/Li⁺F⁻, both holes and electrons are localized in the CN layers, and both exhibit rapid transport in the in-plane direction. The CBM of CN layers consists of both C atoms and N atoms, while the VBM only contains N atoms. Consequently, electrons are subject to more interlayer interactions. From Figures S8a−c and S9a, it is evident in the band structures that the CBM shows stronger dispersion along the Γ−A, M−L, and K−H paths compared to the VBM. Therefore, in these systems, electrons exhibit faster vertical transport than holes.

In systems of PTI/Li⁺Cl⁻, PTI/Li⁺Br⁻, and PTI/Li⁺I⁻, electrons demonstrate a distinct advantage in the in-plane direction, while holes exhibit a notable advantage in the vertical direction. From Figures S8d−f and S9b−d, it can be noted that the VBM exhibits almost negligible dispersion within the in-plane directions, in the out-of-plane directions, along the G-A, M-L, and K-H paths; it demonstrates a remarkably strong dispersion relationship. In these systems, the Li-X chains are separated by the triazines; thus, the transport of holes is limited in the pore and shows a fast vertical transport capability. As the size of the anions increases, the anisotropy of electrons and holes becomes more pronounced. The increase of the interlayer spacing and the attenuation of the $\pi−\pi$ interaction reduce the band dispersion along the out-of-plane directions; the transport of electrons between the layers is hindered, and the transport along the in-plane direction is enhanced. Meanwhile, the introduction of trap states by large halogens modifies the band dispersion, and thereby the effective masses, leading to an increase in the transport of holes along the direction of the Li-X chain. In addition, it is interesting to note that the distribution of holes converges to 70% in Li−Cl and 30% in CN layers. Consequently, in PTI/Li⁺Cl⁻, holes exhibit an additional pathway for transfer along the CN layers toward the {10$\bar{1}$0} facet. This may be one of the reasons why PTI/Li⁺Cl⁻ exhibits a superior photocatalytic effect than PTI/Li⁺Br⁻.

Niu and Li and Sun et al. highlighted the potential of PTI as a facet junction.[7,33] The two exposed facets of the hexagonal crystal ({0001} and {10$\bar{1}$0}) can act as distinct types of active centers, helping to suppress reverse reactions and thereby enhance the efficiency of catalytic reactions. The different directions of electron and hole transport assist in directing them to different facets. In PTI/Li⁺X⁻, holes transported vertically migrate more easily to the {0001} facet, while electrons favor the {10$\bar{1}$0} facet. The final destination of charge carrier migration depends on a variety of factors such as the specific environment at the surface. Many studies have reported that PTI/Li⁺Cl⁻ exhibits photocatalytic activity on its {10$\bar{1}$0} facet, where photoexcited electrons have been consistently observed to migrate readily toward the side facets. Instead, studies of the {0001} facet or hole dynamics have been less reported. Our research reveals a distinct anisotropy in the behavior of electrons and holes within PTI/Li⁺X⁻, providing a foundation for the preparation of PTI as a crystalline facet junction. Various factors may account for the inability of holes to reach the {0001} facet under the experimental conditions. For instance, the customary practice of rinsing crystals with water might result in the loss of surface ions, or the outermost CN layer could hinder the contact

between cocatalysts and ions. We suggest that modulation of the surface, such as defect engineering or adjustment of ion distribution, could potentially facilitate the induction of holes to the {0001} facet. This would establish the {0001} facet as an oxidative center, thereby achieving separation of redox-active sites.

CONCLUSIONS

In summary, by performing NAMD simulations, we demonstrate that the intercalated ions in PTI have the potential to separate electrons and holes, thereby prolonging the *e-h* recombination time of PTI. One important factor is the energy level of the trap state introduced by the intercalated anion. The anion with too low energy level cannot serve as the hole trapping center to effectively separate the electron and hole, as observed in PTI/Li$^+$F$^-$, while too deep trap state results in small energy gaps and accelerate the recombination, as is the case with PTI/Li$^+$I$^-$. In addition, anion sizes close to the CN layer interlayer spacing can reduce the interaction between Li-X and CN layers, which is conducive to the fast dephasing between holes located in anions and electrons located in the CN layer during the *e-h* recombination, prolonging the carrier's lifetime, as is the case with PTI/Li$^+$Cl$^-$ and PTI/Li$^+$Br$^-$. The low correlation between Li-X and the CN layer indicates that the modifications of Li-X have little effect on the CN layer, which allows us to maintain the chemical properties of the CN part in PTI when improving the carrier properties by regulating the ions. In addition, the separated electron holes exhibit anisotropy in transport. The holes trapped by anions are mainly transported in the vertical direction, while the electrons remain in the CN layers possess the in-plane transport capability and interlayer distance related vertical transport capability. In the facet junction engineering of PTI-type CNs, the directional differences in the transport capabilities of electrons and holes help to induce electrons and holes to two different crystal facets of PTI, respectively. This opens up a new avenue for improving the photocatalytic performance of PTI. Among the systems of PTI we studied in this work, the Cl$^-$ anion in PTI/Li$^+$Cl$^-$ is suitably sized and the introduced hole trap state has a shallow energy level. Consequently, PTI/Li$^+$Cl$^-$ demonstrates an excellent photoelectric performance, as reported in many experimental studies.

The results demonstrate the potential of PTI/Li$^+$X$^-$ frameworks for charge separation and extending the carrier's lifetime, showing that the photoelectric performance of PTI-type CNs can be enhanced by screening suitable ion species. Modifications to the surface of PTI may unlock the potential of PTI as a faceted junction. Furthermore, changing the types and locations of cations in PTI may also improve its photoelectric performance, and structures similar to PTI, such as PHI formed by the polycondensation of heptazine instead of triazine, may also have similar potential. This reveals that the framework structure of PTI/Li-X has great potential. The simulations in this work provide a valuable theoretical reference for improving the photoelectric properties of these new types of CNs.

ASSOCIATED CONTENT

ⓈⒾ Supporting Information

The Supporting Information is available free of charge at https://pubs.acs.org/doi/10.1021/jacsau.4c00216.

Description of binding energy and kinetics models; structures, electronic structures, and NAMD results of PTI/Li$^+$X$^-$ (PDF)

AUTHOR INFORMATION

Corresponding Author

Wei Lin − *State Key Laboratory of Photocatalysis on Energy and Environment, College of Chemistry, Fuzhou University, Fuzhou 350108, P.R. China; Fujian Provincial Key Laboratory of Theoretical and Computational Chemistry, Xiamen University, Xiamen 361005, P.R. China;* ⓘ orcid.org/0000-0002-5046-4765; Email: wlin@fzu.edu.cn

Author

Xu Cai − *State Key Laboratory of Photocatalysis on Energy and Environment, College of Chemistry, Fuzhou University, Fuzhou 350108, P.R. China*

Complete contact information is available at:
https://pubs.acs.org/10.1021/jacsau.4c00216

Author Contributions

CRediT: **Xu Cai** data curation, formal analysis, investigation, software, writing-original draft; **Wei Lin** conceptualization, funding acquisition, investigation, supervision, validation, writing-review & editing.

Notes

The authors declare no competing financial interest.

REFERENCES

(1) Wang, X.; Maeda, K.; Thomas, A.; Takanabe, K.; Xin, G.; Carlsson, J. M.; Domen, K.; Antonietti, M. A Metal-Free Polymeric Photocatalyst for Hydrogen Production from Water under Visible Light. *Nat. Mater.* **2009**, *8* (1), 76−80.

(2) Zhang, Z.; Leinenweber, K.; Bauer, M.; Garvie, L. A. J.; McMillan, P. F.; Wolf, G. H. High-Pressure Bulk Synthesis of Crystalline C$_6$N$_9$H$_3$·HCl: A Novel C$_3$N$_4$ Graphitic Derivative. *J. Am. Chem. Soc.* **2001**, *123* (32), 7788−7796.

(3) Bojdys, M. J.; Müller, J.-O.; Antonietti, M.; Thomas, A. Ionothermal Synthesis of Crystalline, Condensed, Graphitic Carbon Nitride. *Chem. - Eur. J.* **2008**, *14* (27), 8177−8182.

(4) Lin, L.; Yu, Z.; Wang, X. Crystalline Carbon Nitride Semiconductors for Photocatalytic Water Splitting. *Angew. Chem., Int. Ed.* **2019**, *58* (19), 6164−6175.

(5) Miller, T. S.; Suter, T. M.; Telford, A. M.; Picco, L.; Payton, O. D.; Russell-Pavier, F.; Cullen, P. L.; Sella, A.; Shaffer, M. S. P.; Nelson, J.; Tileli, V.; McMillan, P. F.; Howard, C. A. Single Crystal, Luminescent Carbon Nitride Nanosheets Formed by Spontaneous Dissolution. *Nano Lett.* **2017**, *17* (10), 5891−5896.

(6) Lin, L.; Lin, Z.; Zhang, J.; Cai, X.; Lin, W.; Yu, Z.; Wang, X. Molecular-Level Insights on the Reactive Facet of Carbon Nitride Single Crystals Photocatalysing Overall Water Splitting. *Nat. Catal.* **2020**, *3* (8), 649−655.

(7) Niu, P.; Li, L. Overall Photocatalytic Water Splitting of Crystalline Carbon Nitride with Facet Engineering. *Chem.* **2020**, *6* (10), 2439−2441.

(8) Liu, M.; Wei, C.; Zhuzhang, H.; Zhou, J.; Pan, Z.; Lin, W.; Yu, Z.; Zhang, G.; Wang, X. Fully Condensed Poly (Triazine Imide)

Crystals: Extended π-Conjugation and Structural Defects for Overall Water Splitting. *Angew. Chem., Int. Ed.* **2022**, *61* (2), No. e202113389.

(9) Wirnhier, E.; Döblinger, M.; Gunzelmann, D.; Senker, J.; Lotsch, B. V.; Schnick, W. Poly(Triazine Imide) with Intercalation of Lithium and Chloride Ions $[(C_3N_3)_2(NHxLi_{1-x})_3 \cdot LiCl]$: A Crystalline 2D Carbon Nitride Network. *Chem. − Eur. J.* **2011**, *17* (11), 3213−3221.

(10) Mesch, M. B.; Bärwinkel, K.; Krysiak, Y.; Martineau, C.; Taulelle, F.; Neder, R. B.; Kolb, U.; Senker, J. Solving the Hydrogen and Lithium Substructure of Poly(Triazine Imide)/LiCl Using NMR Crystallography. *Chem. − Eur. J.* **2016**, *22* (47), 16878−16890.

(11) Liao, C.-Z.; Lau, V. W.; Su, M.; Ma, S.; Liu, C.; Chang, C.-K.; Sheu, H.-S.; Zhang, J.; Shih, K. Unraveling the Structure of the Poly(Triazine Imide)/LiCl Photocatalyst: Cooperation of Facile Syntheses and a Low-Temperature Synchrotron Approach. *Inorg. Chem.* **2019**, *58* (23), 15880−15888.

(12) Wang, W.; Cui, J.; Sun, Z.; Xie, L.; Mu, X.; Huang, L.; He, J. Direct Atomic-Scale Structure and Electric Field Imaging of Triazine-Based Crystalline Carbon Nitride. *Adv. Mater.* **2021**, *33* (48), 2106359.

(13) Pauly, M.; Kröger, J.; Duppel, V.; Murphey, C.; Cahoon, J.; Lotsch, B. V.; Maggard, P. A. Unveiling the Complex Configurational Landscape of the Intralayer Cavities in a Crystalline Carbon Nitride. *Chem. Sci.* **2022**, *13* (11), 3187−3193.

(14) Genoux, A.; Pauly, M.; Rooney, C. L.; Choi, C.; Shang, B.; McGuigan, S.; Fataftah, M. S.; Kayser, Y.; Suhr, S. C. B.; DeBeer, S.; Wang, H.; Maggard, P. A.; Holland, P. L. Well-Defined Iron Sites in Crystalline Carbon Nitride. *J. Am. Chem. Soc.* **2023**, *145* (38), 20739−20744.

(15) Chong, S. Y.; Jones, J. T. A.; Khimyak, Y. Z.; Cooper, A. I.; Thomas, A.; Antonietti, M.; Bojdys, M. J. Tuning of Gallery Heights in a Crystalline 2D Carbon Nitride Network. *J. Mater. Chem. A* **2013**, *1* (4), 1102−1107.

(16) Burmeister, D.; Müller, J.; Plaickner, J.; Kochovski, Z.; List-Kratochvil, E. J. W.; Bojdys, M. J. Size Effects of the Anions in the Ionothermal Synthesis of Carbon Nitride Materials. *Chem. − Eur. J.* **2022**, *28* (33), No. e202200705.

(17) Burmeister, D.; Tran, H. A.; Müller, J.; Guerrini, M.; Cocchi, C.; Plaickner, J.; Kochovski, Z.; List-Kratochvil, E. J. W.; Bojdys, M. J. Optimized Synthesis of Solution-Processable Crystalline Poly-(Triazine Imide) with Minimized Defects for OLED Application. *Angew. Chem., Int. Ed.* **2022**, *61* (3), No. e202111749.

(18) Wang, Q.; Gao, Q.; Al-Enizi, A. M.; Nafady, A.; Ma, S. Recent Advances in MOF-Based Photocatalysis: Environmental Remediation under Visible Light. *Inorg. Chem. Front.* **2020**, *7* (2), 300−339.

(19) Liu, S.; Guo, R.; Xie, F. The Effects of Organic Cation Rotation in Hybrid Organic-Inorganic Perovskites: A Critical Review. *Mater. Des.* **2022**, *221*, No. 110951.

(20) Zheng, Q.; Chu, W.; Zhao, C.; Zhang, L.; Guo, H.; Wang, Y.; Jiang, X.; Zhao, J. Ab Initio Nonadiabatic Molecular Dynamics Investigations on the Excited Carriers in Condensed Matter Systems. *WIREs Comput. Mol. Sci.* **2019**, *9* (6), No. e1411.

(21) Kresse, G.; Hafner, J. Ab Initio Molecular Dynamics for Liquid Metals. *Phys. Rev. B* **1993**, *47* (1), 558−561.

(22) Kresse, G.; Hafner, J. Ab Initio Molecular-Dynamics Simulation of the Liquid-Metalamorphous- Semiconductor Transition in Germanium. *Phys. Rev. B* **1994**, *49* (20), 14251−14269.

(23) Kresse, G.; Furthmüller, J. Efficient Iterative Schemes for Ab Initio Total-Energy Calculations Using a Plane-Wave Basis Set. *Phys. Rev. B* **1996**, *54*, 11169−11186.

(24) Kresse, G.; Joubert, D. From Ultrasoft Pseudopotentials to the Projector Augmented-Wave Method. *Phys. Rev. B - Condens. Matter Mater. Phys.* **1999**, *59* (3), 1758−1775.

(25) Perdew, J. P.; Burke, K.; Ernzerhof, M. Generalized Gradient Approximation Made Simple. *Phys. Rev. Lett.* **1996**, *77* (18), 3865−3868.

(26) Krukau, A. V.; Vydrov, O. A.; Izmaylov, A. F.; Scuseria, G. E. Influence of the Exchange Screening Parameter on the Performance of Screened Hybrid Functionals. *J. Chem. Phys.* **2006**, *125* (22), 224106.

(27) Jaeger, H. M.; Fischer, S.; Prezhdo, O. V. Decoherence-Induced Surface Hopping. *J. Chem. Phys.* **2012**, *137* (22), 22A545.

(28) Qiao, L.; Fang, W.-H.; Long, R.; Prezhdo, O. V. Elimination of Charge Recombination Centers in Metal Halide Perovskites by Strain. *J. Am. Chem. Soc.* **2021**, *143* (26), 9982−9990.

(29) Chi, H.-Y.; Chen, C.; Zhao, K.; Villalobos, L. F.; Schouwink, P. A.; Piveteau, L.; Marshall, K. P.; Liu, Q.; Han, Y.; Agrawal, K. V. Unblocking Ion-Occluded Pore Channels in Poly(Triazine Imide) Framework for Proton Conduction. *Angew. Chem.* **2022**, *134* (40), No. e202207457.

(30) Ham, Y.; Maeda, K.; Cha, D.; Takanabe, K.; Domen, K. Synthesis and Photocatalytic Activity of Poly(Triazine Imide). *Chem. - Asian J.* **2013**, *8* (1), 218−224.

(31) Steinmann, S. N.; Melissen, S. T. A. G.; Le Bahers, T.; Sautet, P. Challenges in Calculating the Bandgap of Triazine-Based Carbon Nitride Structures. *J. Mater. Chem. A* **2017**, *5* (10), 5115−5122.

(32) Melissen, S.; Le Bahers, T.; Steinmann, S. N.; Sautet, P. Relationship between Carbon Nitride Structure and Exciton Binding Energies: A DFT Perspective. *J. Phys. Chem. C* **2015**, *119* (45), 25188−25196.

(33) Sun, S.; He, L.; Yang, M.; Cui, J.; Liang, S. Facet Junction Engineering for Photocatalysis: A Comprehensive Review on Elementary Knowledge, Facet-Synergistic Mechanisms, Functional Modifications, and Future Perspectives. *Adv. Funct. Mater.* **2022**, *32* (1), 2106982.